

Wire Arc Additive Manufactured CuMn13Al7 High-Manganese Aluminium Bronze

Chun Guo

Anhui Science and Technology University

Bai-Song Hu

Anhui Science and Technology University

Bao-Li Wei (✉ ahstu2762@outlook.com)

Anhui Science and Technology University

Feng Chen

Anhui Science and Technology University

Original Article

Keywords: CuMn13Al7, high-manganese aluminium bronze, wire arc additive manufacturing, microstructure, mechanical properties

Posted Date: May 5th, 2020

DOI: <https://doi.org/10.21203/rs.3.rs-25507/v1>

License:  This work is licensed under a Creative Commons Attribution 4.0 International License.

[Read Full License](#)

Abstract

In this work, high-manganese aluminium bronze $\text{CuMn}_{13}\text{Al}_7$ samples were prepared by arc additive manufacturing technology. The phase composition, microstructure, and crystal structure of the high-manganese aluminium bronze $\text{CuMn}_{13}\text{Al}_7$ arc additive manufactured samples were analysed using direct-reading spectrometer, metallographic microscope, scanning electron microscope, and transmission electron microscope. The micro-hardness tester, tensile tester, impact tester, and electrochemical workstation were also used to test the performance of the $\text{CuMn}_{13}\text{Al}_7$ samples. By studying the microstructure and properties of the $\text{CuMn}_{13}\text{Al}_7$ samples, it was found that preparation of the samples by the arc additive manufacturing technology ensured good forming quality, almost no defects, and good metallurgical bonding inside the sample. The metallographic structure ($\alpha + \beta +$ point phase) mainly comprises the following: the metallographic structure in the equiaxed grain region has an obvious grain boundary α ; the metallographic structure in the remelting region has no obvious grain boundary α ; the thermal influence on the metallographic structure produced a weaker grain boundary α than the equiaxed grain region. The transverse and longitudinal cross sections of the sample had uniform microhardness distributions, and the average microhardness values were $190.5 \text{ HV}_{0.1}$ and $192.7 \text{ HV}_{0.1}$, respectively. The sample also had excellent mechanical properties: yield strength of 301 MPa, tensile strength of 633 MPa, elongation of 43.5%, reduction of area by 58%, Charpy impact value of 68 J at -20°C , and dynamic potential polarisation curve test results. Further, it was shown that the average corrosion potential of the sample was -284.5 mV , and the average corrosion current density was $4.1 \times 10^{-3} \text{ mA/cm}^2$.

1 Introduction

Additive manufacturing is also called as three-dimensional (3D) printing and is different from traditional subtractive (cutting) processing technologies as it uses a 3D data model of the parts[1-4]. Based on the principle of discrete layering or stacking, different heat sources (laser beam, ion beam, electron beam, arc, ultraviolet light, etc.) are used to apply raw materials (powder, wire, liquid materials, etc.) in a layer by layer manner to manufacture parts. Compared with traditional processing technologies, additive manufacturing has outstanding features, including short manufacturing cycle, lower production costs for some parts, high material utilisation, high degree of design/manufacturing integration, and design of component structure. Optimisation techniques available in this process are especially suitable for manufacturing parts and components with complex structures and high added value of raw materials. Additive manufacturing thus has broad prospects in aviation, aerospace, automotive, biomedical, educational, and mould manufacturing applications, among others [5-9].

Additive manufacturing technology is mainly divided into metal and non-metallic additive manufacturing based on the types of materials used. Metal additive manufacturing technologies mainly include laser, electron beam, plasma, and electric arc additive manufacturing based on the heat source [10-13]. Compared with other additive manufacturing technologies, arc additive manufacturing has high production efficiency and is suitable for large-scale component manufacturing[14]. The disadvantage of

using electric arc as the heat source is that the manufacturing accuracy is not as good as that obtained with lasers and electron beams [15-18]. Arc additive manufacturing technology has received widespread attention in aerospace, mechanical equipment production and other fields in recent years [19-21].

High-manganese aluminium bronze is a high-strength copper alloy that is based on ordinary aluminium bronze. By adding multiple elements such as manganese, aluminium, iron, nickel, and titanium and with rare earth modification treatment, the matrix structure is strengthened. The phases are uniformly distributed in a tough matrix, and a type of alloy is formed with enhanced strength without reduction of plasticity. High-manganese aluminium bronze materials have high strength, hardness, toughness, and wear resistance, and their comprehensive mechanical properties are reported to be good [22, 23]. The high-manganese aluminium bronze material has good corrosion resistance when exposed to the atmosphere, fresh water, and seawater. It resists high-speed seawater erosion and has high corrosion fatigue strength. Because the high-manganese aluminium bronze material has a higher electrode potential, the surface energy is important. A strong alumina film is formed, and if this film is damaged, it can be self-healed as well as re-formed and covered, so that the corrosion resistance is improved [24]. Further, high-manganese aluminium bronze alloys have good casting properties and can be welded. Therefore, high-manganese aluminium bronze materials are one of the main materials used in large propellers in various countries around the world. Manganese aluminium bronze materials are also widely used in steel rolling equipment and other metallurgical machinery to manufacture sliders, slides, bearings, bushings, nuts, etc. (generally referred to as metallurgical spare parts), which can adequately meet the requirements of production conditions [25, 26]. However, cast high-manganese aluminium bronze suffers from reduced seawater corrosion resistance owing to the coarse structure, component segregation, and casting defects [27]. Therefore, it is of great significance to research new manufacturing processes for high-manganese aluminium bronze parts.

To the best of the authors' knowledge, there are no reports on research involving additive manufacturing of high-manganese aluminium bronze. Therefore, this study uses the arc additive manufacturing technology and $\text{CuMn}_{13}\text{Al}_7$ welding wire to investigate high-manganese aluminium bronze arc additive manufacturing technology. It is expected that this study can provide theoretical and data support for popularisation and application of the additive manufacturing technology.

2 Experimental Setup And Analysis Procedure

The wire used in these experiments was a high-manganese aluminium bronze $\text{CuMn}_{13}\text{Al}_7$ supporting welding material produced by Newland (Tianjin) Welding Material Co., Ltd., with a grade of $\text{CuMn}_{13}\text{Al}_7$ M and diameter of 1.2 mm. The arc additive manufacturing equipment uses TPS4000 cold metal transfer (CMT) advanced power supply, KUKA six-axis robot KR 10R1420 and lungoPNT robot arc additive manufacturing software. The experimental substrate was Q235 steel of dimensions 300 mm × 100 mm × 12 mm. Before the experiment, the substrate was polished with a hand-held grinding wheel to remove rust and scale on the surface of the steel plate. In order to reduce the amount of deformation of the substrate during the additive manufacturing process, the steel plate was fixed to the base steel plate using a

designed fixture. In this research, the arc additive manufacturing process adopts the CMT mode, and single-layer single-pass, single-layer multi-pass, and multi-layer multi-pass tests are performed in the early stages of testing; further, the preferred additive manufacturing process parameters are selected according to the shape of the bead. In order to control the forming accuracy of the additive manufacturing sample, a Fluke F59 infrared thermometer was used to detect the interlayer temperature during the manufacturing process. The process parameters selected for this research are as follows: current 115 A, voltage 11.4 V, wire feed speed 4.5 m/min, shielding gas 100% Ar, shielding gas flow 18 L/min, and interlayer temperature not exceeding 150 °C. The specific process parameters are summarised in Table 2.

The size of the printed sample (thin wall) using arc additive manufacturing in this research is approximately 150 mm × 20 mm × 60 mm. Using a band saw and wire cutters, samples were obtained from the middle of the manufactured sample for metallographic analysis (hardness test, scanning electron microscopy (SEM) analysis), transmission electron microscopy (TEM), and chemical composition analysis. Tensile tests were conducted on both sides of the sample in directions parallel and perpendicular to the deposition direction and on impact specimens. The chemical composition analysis test was carried out according to GB/T 4336-2016, using a QSN750 direct-reading spectrometer. The tensile tests of the sample were carried out according to the standard GB/T228.1-2010. The room temperature tensile performance was evaluated using a 100 kN material testing machine (SINTECH20 / G). Displacement control was used during the stretching, and the initial strain rate of the sample was 0.005 min⁻¹. The sample impact test was performed according to GB/T229-2007 using a pendulum impact tester (ZBC2302-C); the test temperature was -50 °C, and three samples were tested in each group. The metallographic and SEM samples were cut, ground, and polished, and then etched with a saturated iron nitrate alcohol solution. The OLYMPUS GX71 metallographic microscope was used to observe the microstructure of the metallographic samples based on the standard GB/T 13298-2015 "Metal microstructure inspection method". ZEISS EVO-18 and Quanta650 scanning electron microscope were used to observe the microstructure of the metallographic sample at high magnification and corrosion morphology after the electrochemical corrosion test, respectively. The Genesis Apex2 X-ray spectrometer attached to the scanning electron microscope was used for component analysis. The TEM sample was cut from a 0.5 mm slice from the block sample, and ground to a thickness of about 120 µm; three wafers were punched out, and finely ground to about 50 µm. A 4% perchloric acid solution was used as the electrolyte, and a perforated film sample was obtained by double-spray electrolysis at -20 °C. The electrolysis voltage was set to 75 V, and the Gatan691 ion thinner was used on the argon ions for 0.5 h to reduce their thickness. The TEM sample was used to observe the crystal structure with a JEM-2100 transmission electron microscope, and the acceleration voltage was 200 kV. According to the GB/T 4340.1-2009 "Vickers hardness test for metallic materials-Part 1: Test method" standard, the micro Vickers hardness is measured with a test force of 100 g, and the tests are conducted from the upper part of the weld (2 mm) to the lower part. Ten points were measured at equal distances (1 mm apart), and a microhardness tester VMH-104 was used. The Gill AC Bi-STAT electrochemical workstation was used to test the polarisation curves of the samples; the test conditions were room temperature (~25 °C) and 3.5% NaCl aqueous solution (neutral). After the sample was connected to the wire, it was sealed with a sealant,

and a surface of 10 mm × 10 mm was reserved as the test surface. Before the test, the surface was polished with sandpaper until there were no obvious scratches on the surface. The three-electrode system was used for the test: the reference electrode was a saturated calomel electrode, a platinum electrode was the auxiliary electrode, and the sample was the working electrode (the potentials in the report are relative to the saturated calomel electrode unless specified otherwise). First the open-circuit potential was measured for 30 min, and then the potentiodynamic polarisation curve test was performed. When the polarisation curve was tested, the scanning range used was -150 to +600 mV (relative to the open-circuit potential), and the scanning rate was 20 mV/min. After completion of the test, the results were processed with software to obtain the final data.

Table 1 Chemical composition (wt%) of the CuMn₁₃Al₇ wire

Sample	Al	Fe	Mn	Ni	Cu
CuMn ₁₃ Al ₇	7.29	2.19	11.91	1.96	Balance

Table 2 Wire arc additive manufacturing parameters

Diameter (mm)	Voltage (V)	Current (A)	Wire-feed speed (m·min ⁻¹)	Printing speed (m·s ⁻¹)	Contact tip to work distance (mm)	Shielding gas flow (L·min ⁻¹)	Interpass temperature (°C)	Overlap rate (%)
1.2	11.4	115	4.5	12	15	18	≤150	50

3 Results And Discussion

3.1 CuMn₁₃Al₇ additive manufacturing forming characteristics

Figure 1 shows a sample of the CuMn₁₃Al₇ thin wall printed by arc additive manufacturing technology. It can be seen from the sample picture that the thin-walled CuMn₁₃Al₇ printed by the CMT power supply is adequately formed without collapse, and the welding wire splashing is small during the forming process. In addition, from the sample cross-sectional view (metallographic sample) given in Figure 2, it can be seen that there are almost no defects inside the sample and that the metallurgical bonding is good, which further illustrates that CuMn₁₃Al₇ has good forming performance by arc additive manufacturing.

3.2 High-manganese aluminium bronze CuMn₁₃Al₇ additive manufacturing composition and microstructure characteristics

Table 3 shows the chemical composition analysis results of the high-manganese aluminium bronze CuMn₁₃Al₇ arc additive manufacturing samples. Compared to the chemical composition of the raw silk

materials given in Table 1, it can be seen that the main alloying element Mn in the arc additive manufacturing sample has a burning loss of 6.1%. The decrease in relative content is more pronounced, which indicates that the arc additive manufacturing process has better protection and better deoxidation performance in the molten pool.

Table 3 Chemical composition (wt%) of the CuMn₁₃Al₇ sample formed by wire arc additive manufacturing

Sample	Mn	Ni	Al	Fe	Cu
CuMn ₁₃ Al ₇	11.18	2.32	7.42	2.21	Balance

Figure 3 is an X-ray diffraction (XRD) pattern of a high-manganese aluminium bronze CuMn₁₃Al₇ arc additive manufacturing sample, and the main phase composition of the sample is Cu_{0.69}Al_{0.28}Ni_{0.02} and Cu.

Figure 4 shows the metallographic pictures of the high-manganese aluminium bronze CuMn₁₃Al₇ arc additive manufacturing samples at different locations. The low magnification metallographic structure is shown in Fig. 4 (a), and the equiaxed crystal region is shown below that. The entire sample is mainly composed of equiaxed crystal regions, and there are fewer columnar crystals. The middle strip is the remelting zone, and the heat-affected zone is above the remelting zone. From Fig. 4 (b) and Fig. 4 (c), it can be seen that the metallographic structure of the equiaxed grain region of the high-manganese aluminium bronze CuMn₁₃Al₇ arc additive manufacturing sample is $\alpha + \beta +$ point phase, and the grain boundary α is obvious. The sample metallographic structure in the remelting zone is $\alpha + \beta +$ point phase with no obvious grain boundary α (see Figs. 4 (d) and 4 (e)). The metallographic structure of the sample heat-affected zone is $\alpha + \beta +$ dot-like phase, and the grain boundary α is weaker than that in the equiaxed grain region (see upper part in Figs. 4 (d) and 4 (f)). In addition, it can be seen from the low magnification metallographic photograph in Fig. 4 (a) that no cracks, holes, solid inclusions, unfused, unwelded, poorly shaped or sized, and other defects are found, indicating that the internal quality of the CuMn₁₃Al₇ steel arc additive manufacturing is good. Figure 5 shows a high magnification SEM image of the metallographic sample. No small defects were found in the high magnification SEM image. The sample mainly had a fine needle-like structure inside the equiaxed crystal region under high magnification SEM.

To further analyse the crystal structure of the high-manganese aluminium bronze CuMn₁₃Al₇ arc additive manufacturing sample, Fig. 6 shows the TEM image of the sample and the EDS composition of the corresponding particles. From the TEM image (Fig. 6 (a)), it can be seen that there is a granular reinforcing phase in the slab-like matrix of the sample crystal structure at high magnification. The EDS analysis results corresponding to Figs. 6 (b) to 6 (e) show that the main elemental composition of the large particle reinforcing phase is Fe, Mn, Al, and the main elemental composition of the small particle reinforcing phase is Cu, Mn, Fe, Al. The light and dark matrix phases are mainly composed of Cu, Mn, Al, and Fe, which are consistent with the elemental composition of the samples obtained by chemical analysis.

Figure 7 shows the crystal structure and corresponding selected area electron diffraction pattern of the high-manganese aluminium bronze $\text{CuMn}_{13}\text{Al}_7$ arc additive manufacturing sample. Figure 7 (a) is a high-magnification image of the large particle enhanced phase in Fig. 6 (a) and the corresponding selected area electron diffraction pattern. From the analysis of the pattern, it can be seen that the corresponding phase is the Fe_2MnAl phase. The EDS elemental composition results of the large particle enhanced phase are consistent, but there is no obvious Fe_2MnAl phase diffraction peak in the XRD pattern of the sample in Figure 3. This may be attributable to the fact that XRD analysis is generally considered for phases with a relative content of less than 5%. The diffraction peak is not seen clearly in the entire spectrum, so no Fe_2MnAl phase was found in the XRD pattern of the sample. Figure 7 (b) shows the morphology of the matrix phase and the corresponding selected area electron diffraction pattern. From the analysis of the results, it can be seen that the corresponding phase is $\text{Cu}_{0.69}\text{Al}_{0.28}\text{Ni}_{0.02}$, which is in accordance with the XRD (Figure 3) results and the figure of the sample. The results obtained from the analysis of Figs. 6 (c) and 6 (e) are also completely consistent in this regard. In addition, TEM analysis revealed that particle-reinforced phases + twins (Fig. 8 (a)) and particle-reinforced phases + dislocations (Fig. 8 (b)), particle-reinforced phases, twins, and dislocations also existed in the sample. The appearance of such components is beneficial for increasing the strength of the sample.

3.3 Performance of high-manganese aluminium bronze $\text{CuMn}_{13}\text{Al}_7$ additive manufacturing samples

Figure 9 shows the microhardness distribution of the high-manganese aluminium bronze $\text{CuMn}_{13}\text{Al}_7$ arc additive manufacturing samples. During the test, measurements are obtained from the upper part of the weld (2 mm) to the lower part, and from the left (2 mm) to the right. Results were obtained at 10 uniformly spaced points (1 mm apart). From the microhardness distribution chart, it can be seen that the hardness distribution of the high-manganese aluminium bronze $\text{CuMn}_{13}\text{Al}_7$ arc additive manufacturing sample ranges from 173 to 220 $\text{HV}_{0.1}$, and the hardness distribution is relatively uniform. The average microhardness of the longitudinal cross section of the sample is 192.7 $\text{HV}_{0.1}$, the average microhardness of the transverse cross section of the sample is 190.5 $\text{HV}_{0.1}$, and the difference between the average microhardness of the longitudinal and transverse cross sections is small. The fluctuation of the microhardness is mainly caused by the change in the microstructure. From the cross-sectional morphology of the high-manganese aluminium bronze $\text{CuMn}_{13}\text{Al}_7$ formed sample produced by arc additive manufacturing shown in Fig. 2, it can be seen that the formed sample is a multi-layer and multi-pass surfaced structure. The effects of thermal cycling of the weld bead generally includes the original columnar crystal zone, remelting zone, and heat-affected zone. Different regions have different microhardness values owing to different microstructures (grain size, precipitates, etc.), so the sample cross-section hardness is expected to fluctuate by nominal amounts.

Table 4 Mechanical properties of the $\text{CuMn}_{13}\text{Al}_7$ sample formed by wire arc additive manufacturing

Sample	Yield Strength (MPa)	Tensile Strength (MPa)	Elongation (%)	Percentage reduction of area after fracture (%)	-20 °C Impact value (J)
Sample	301	633	43.5	58	68

The test results of the mechanical properties of the high-manganese aluminium bronze CuMn₁₃Al₇ arc additive manufacturing sample are shown in Table 4. From the results, it can be seen that the sample has excellent mechanical properties, yield strength of 301 MPa, tensile strength of 633 MPa, elongation of 43.5%, reduction in area of 58%, and Charpy impact value of 68 J at -20 °C.

In order to analyse the fracture mechanism of the sample, Fig. 10 shows the tensile fracture morphology of the high-manganese aluminium bronze CuMn₁₃Al₇ arc additive manufacturing sample. It can be clearly seen from the overall morphology of the tensile fracture in Fig. 10 (a) that there are no obvious defects in the tensile specimen, which is in accordance with the experimental results of the tensile elongation and section shrinkage of the tensile specimen, as shown in Table 4. Figures 10 (b), 10 (c), and 10 (d) are the morphologies of the tensile fracture fibre zone, radiation zone, and secondary fibre zone, respectively. From the figure, it can be seen that there is a large number of dimples in the fracture, indicating that the sample is stretched. The fracture mechanism is mainly ductile fracturing, and the radiation area has a river-like dissociation surface morphology.

Figure 11 shows the kinetic potential polarisation curve of the sample. It can be seen from the figure that the anodic polarisation curve of the sample is divided into two distinct stages. The anode current density rapidly increases in the interval between the corrosion potential (EC) and point A, indicating that no obvious passivation behaviour has occurred on the sample surface. Controlled by activation and mass transfer processes, the maximum current and slower increase of current in the interval A ~ B indicate that the reaction in this interval is controlled by the mass transfer process. The corrosion potential and corrosion current density of the samples obtained by software fitting are shown in Table 5. Figure 12 shows the corrosion morphology of the sample after the potentiostatic polarisation test. It can be seen from the figure that the electrochemical corrosion mechanism of the sample is mainly intergranular corrosion.

Table 5 Potentiodynamic polarisation results

Sample	Corrosion potential (mV)	Corrosion current density (mA/cm ²)
1#	-291	4.3×10 ⁻³
2#	-278	3.9×10 ⁻³

4 Conclusions

(1) High-manganese aluminium bronze CuMn₁₃Al₇ samples were prepared by the arc additive manufacturing technology. The forming quality of the sample was found to be good, with no large defects being present, and the metallurgical bonding inside the sample was also good. The metallographic structure is mainly the α + β + point phase.

(2) The micro-hardness distribution of the transverse and longitudinal sections of the sample were relatively uniform, and the average micro-hardness values were 190.5 HV_{0.1} and 192.7 HV_{0.1}, respectively. The mechanical properties of the samples were excellent, with yield strength of 301 MPa, tensile strength of 633 MPa, elongation of 43.5%, reduction in area of 58%, and Charpy impact value of 68 J at –20 °C.

(3) The results of the kinetic potential polarisation curve test show that the average corrosion potential of the sample was –284.5 mV and average corrosion current density was 4.1×10^{-3} mA/cm². The research presented in this paper is expected to provide theoretical and data support for the application of additive manufacturing technology in the manufacture of high-manganese aluminium bronze parts in the future.

Declarations

Acknowledgements

The authors sincerely thanks to Professor Hengyao Dang of Luoyang Ship Material Research Institute, China for his critical discussion and reading during manuscript preparation.

Biographical notes

Chun Guo, born in 1984, is currently an associate professor at *Anhui Science and Technology University, China*. He received his PhD degree from *University of Chinese Academy of Sciences, China*, in 2012. His research interests include additive manufacturing, surface engineering and welding.

Tel: +86-550-6734840; E-mail: guochun@ahstu.edu.cn

Bai-Song Hu, born in 1998, is currently a bachelor candidate at *Anhui Science and Technology University, China*.

E-mail: 924549216@qq.com

Bao-Li Wei, born in 1970, is currently an associate professor at *Anhui Science and Technology University, China*. He received his MA degree from *Nanjing Agricultural University, China*, in 2008. His research interests include automobile lightweight, magnesium alloy material forming.

Tel: +86- 550-6732021; E-mail: ahstu2762@outlook.com

Feng Chen, born in 1972, is currently a professor at *Anhui Science and Technology University, China*. He received his PhD degree from *Nanjing University of Science and Technology, China*, in 2012. His research interests include automobile lightweight material forming and intelligent equipment development, sustainable design and manufacturing.

Tel: +86- 550-6732023; E-mail: chenf2563@gmail.com

Funding

Supported by the University Synergy Innovation Program of Anhui Province (GXXT-2019-022), the Natural Science Foundation of Anhui Province (1908085QE174), and the talent program of Anhui Science and Technology University (RCYJ201905) for financial support.

Availability of data and materials

The datasets supporting the conclusions of this article are included within the article.

Authors' contributions

The author' contributions are as follows: Chun Guo was in charge of the research project and the whole trial; Bai-Song Hu assisted with sampling and laboratory analyses; Bao-Li Wei wrote the manuscript; Feng Chen review of existing research works, analysis of the Design and for Additive Manufacturing strategies. All authors read and approved the final manuscript.

Competing interests

The authors declare no competing financial interests.

Consent for publication

Not applicable

Ethics approval and consent to participate

Not applicable

References

- [1] H I.Medellin?Castillo, J Zaragoza?Siqueiros. Design and Manufacturing Strategies for Fused Deposition Modelling in Additive Manufacturing:A Review. *Chinese Journal of Mechanical Engineering*, 2019, 32(03): 13-28.
- [2] M Harnois, M Himdi, W Y Yong, et al. An Improved Fabrication Technique for the 3-D Frequency Selective Surface based on Water Transfer Printing Technology. *Sci Rep*, 2020, 10(1): 1714(1-8).
- [3] D Loterie, P Delrot, C Moser. High-resolution tomographic volumetric additive manufacturing. *Nat Commun*, 2020, 11(1): 852(1-6).
- [4] Z Zou, M Simonelli, J Katrib, et al. Refinement of the grain structure of additive manufactured titanium alloys via epitaxial recrystallization enabled by rapid heat treatment. *Scripta Materialia*, 2020, 180:66-70.
- [5] M J Martín De Vidales, A Nieto-Márquez, D Morcuende, et al. 3D printed floating photocatalysts for wastewater treatment. *Catalysis Today*, 2019, 328:157-163.

- [6] A A Giannopoulos, D Mitsouras, S J Yoo, et al. Applications of 3D printing in cardiovascular diseases. *Nature Reviews Cardiology*, 2016, 13(12): 701-718.
- [7] Y Zhang, F Zhang, Z Yan, et al. Printing, folding and assembly methods for forming 3D mesostructures in advanced materials. *Nature Reviews Materials*, 2017, 2(4): 17019.
- [8] J H Martin, B D Yahata, J M Hundley, et al. 3D printing of high-strength aluminium alloys. *Nature*, 2017, 549(7672): 365-369.
- [9] D Evers. Control architectures for Industrial Additive Manufacturing Systems. *Proceedings of the Institution of Mechanical Engineers, Part B: Journal of Engineering Manufacture*, 2017, 232(10): 1767-1777.
- [10] Z Li, C Liu, T Xu, et al. Reducing arc heat input and obtaining equiaxed grains by hot-wire method during arc additive manufacturing titanium alloy. *Materials Science and Engineering: A*, 2019, 742:287-294.
- [11] A Huang. Electromagnetic Vibration Monitoring Method for Liquid Transfer Mode in Wire Feeding Based Laser Additive Manufacturing(WFLAM). *Journal of Mechanical Engineering*, 2018, 54(2): 34-40.
- [12] X Wang, X Gong, K Chou. Review on powder-bed laser additive manufacturing of Inconel 718 parts. *Proceedings of the Institution of Mechanical Engineers, Part B: Journal of Engineering Manufacture*, 2016, 231(11): 1890-1903.
- [13] G-H Song, S-K Jing, F-L Zhao, et al. Design Optimization of Irregular Cellular Structure for Additive Manufacturing. *Chinese Journal of Mechanical Engineering*, 2017, 30(05): 1184-1192.
- [14] J Xiong, Y-J Li, Z-Q Yin, et al. Determination of Surface Roughness in Wire and Arc Additive Manufacturing Based on Laser Vision Sensing. *Chinese Journal of Mechanical Engineering*, 2018, 31(04): 133-139.
- [15] X Xu, S Ganguly, J Ding, et al. Microstructural evolution and mechanical properties of maraging steel produced by wire + arc additive manufacture process. *Materials Characterization*, 2018, 143:152-162.
- [16] X Chen, J Li, X Cheng, et al. Microstructure and mechanical properties of the austenitic stainless steel 316L fabricated by gas metal arc additive manufacturing. *Materials Science and Engineering: A*, 2017, 703:567-577.
- [17] F Wang, S Williams, P Colegrove, et al. Microstructure and Mechanical Properties of Wire and Arc Additive Manufactured Ti-6Al-4V. *Metallurgical and Materials Transactions A*, 2012, 44(2): 968-977.
- [18] M J Bermingham, L Nicastro, D Kent, et al. Optimising the mechanical properties of Ti-6Al-4V components produced by wire + arc additive manufacturing with post-process heat treatments. *Journal of Alloys and Compounds*, 2018, 753:247-255.

- [19] A Lopez, R Bacelar, I Pires, et al. Non-destructive testing application of radiography and ultrasound for wire and arc additive manufacturing. *Additive Manufacturing*, 2018, 21:298-306.
- [20] X Xu, J Ding, S Ganguly, et al. Oxide accumulation effects on wire + arc layer-by-layer additive manufacture process. *Journal of Materials Processing Technology*, 2018, 252:739-750.
- [21] F Hejripour, D T Valentine, D K Aidun. Study of mass transport in cold wire deposition for Wire Arc Additive Manufacturing. *International Journal of Heat and Mass Transfer*, 2018, 125:471-484.
- [22] X Y Li, Y G Yan, L Ma, et al. Cavitation erosion and corrosion behavior of copper–manganese–aluminum alloy weldment. *Materials Science and Engineering: A*, 2004, 382(1-2): 82-89.
- [23] Tianxiang, G Huang, P Lv, et al. Study on the Formation of Calcareous Deposits on High Manganese Aluminum Bronze by Polarization Potential. *Development and Application of Materials*, 2018, 33(2): 23-32.
- [24] L Jing, Y Yonggui, C Guangzhang. Study on Microbiologically Influenced Corrosion of Copper Manganese Aluminium Alloy. *Rare Metal Materials and Engineering*, 2007, 36(S3): 551-554.
- [25] Q N Song, N Xu, X Jiang, et al. Effect of Sulfide Concentration on the Corrosion and Cavitation Erosion Behavior of a Manganese-Aluminum Bronze in 3.5% NaCl Solution. *Journal of Materials Engineering and Performance*, 2019, 28(7): 4053-4064.
- [26] P Kuppahalli, R Keshavamurthy, P Sriram, et al. Microstructural and Mechanical behaviour of Nickel Aluminum Bronze alloys. *IOP Conference Series: Materials Science and Engineering*, 2019, 577: 012041-012046.
- [27] C He, X Fu, H Chen, et al. Corrosion Resistance of Laser-Clad Copper-Based Alloy on High Manganese Aluminum Bronze Surface. *Journal of Shenyang University (Natural Science)*, 2019, 31(2): 87-91.

Figures

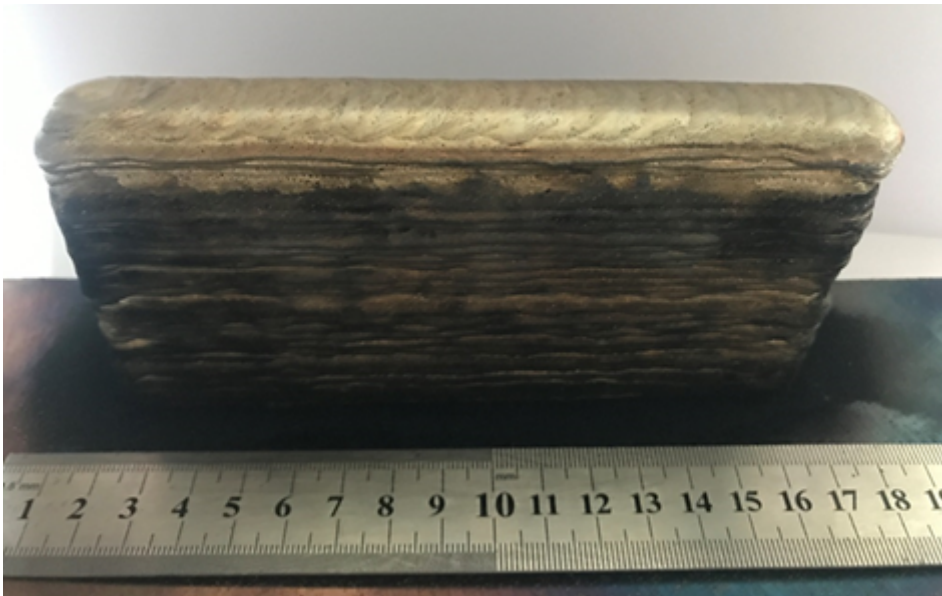


Figure 1

Sample of CuMn13Al7 high-manganese aluminium bronze prepared by wire arc additive manufacturing



Figure 2

Cross-sectional view of the CuMn13Al7 high-manganese aluminium bronze prepared by wire arc additive manufacturing

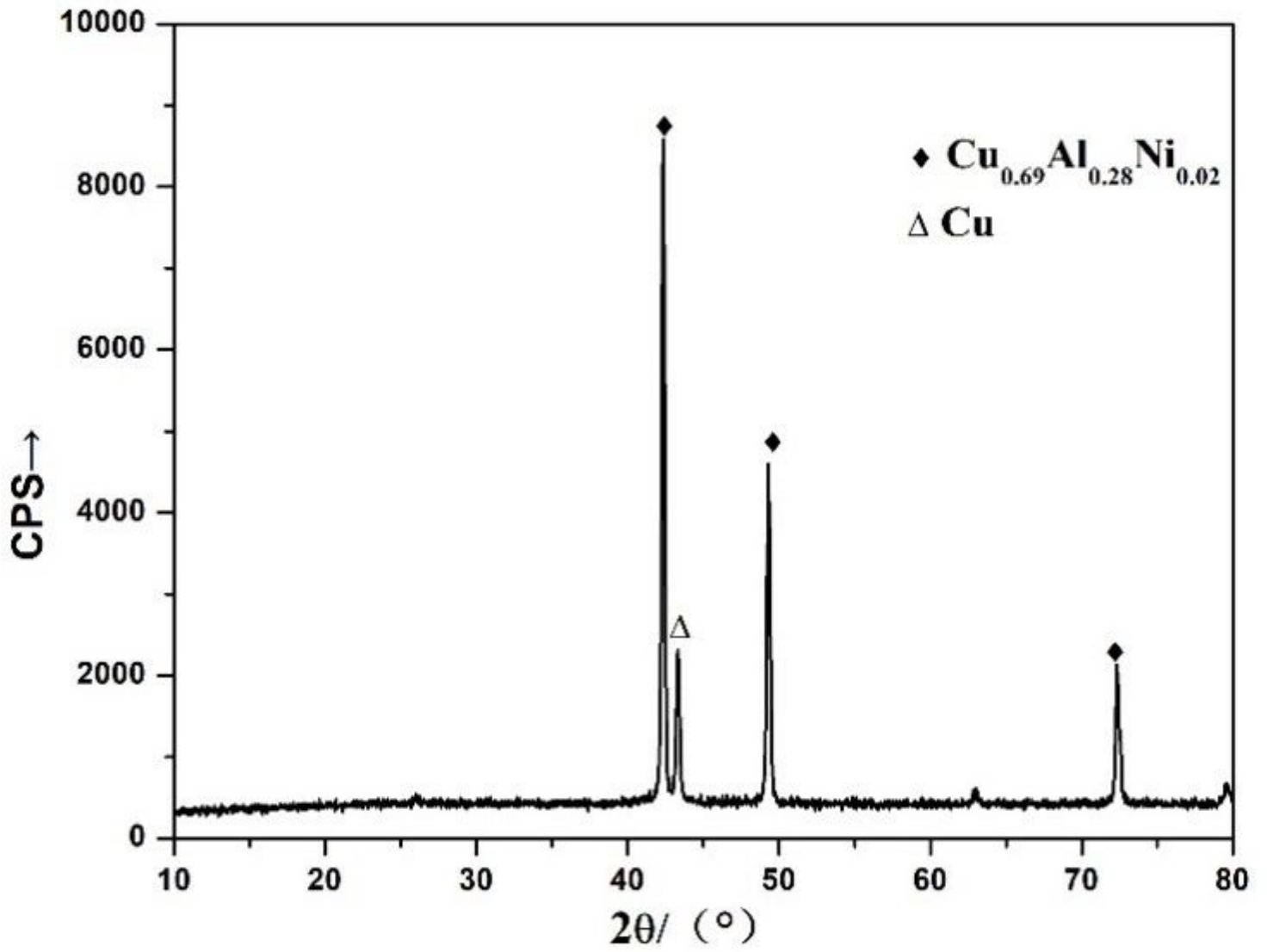


Figure 3

XRD pattern of CuMn13Al7 high-manganese aluminium bronze prepared by wire arc additive manufacturing

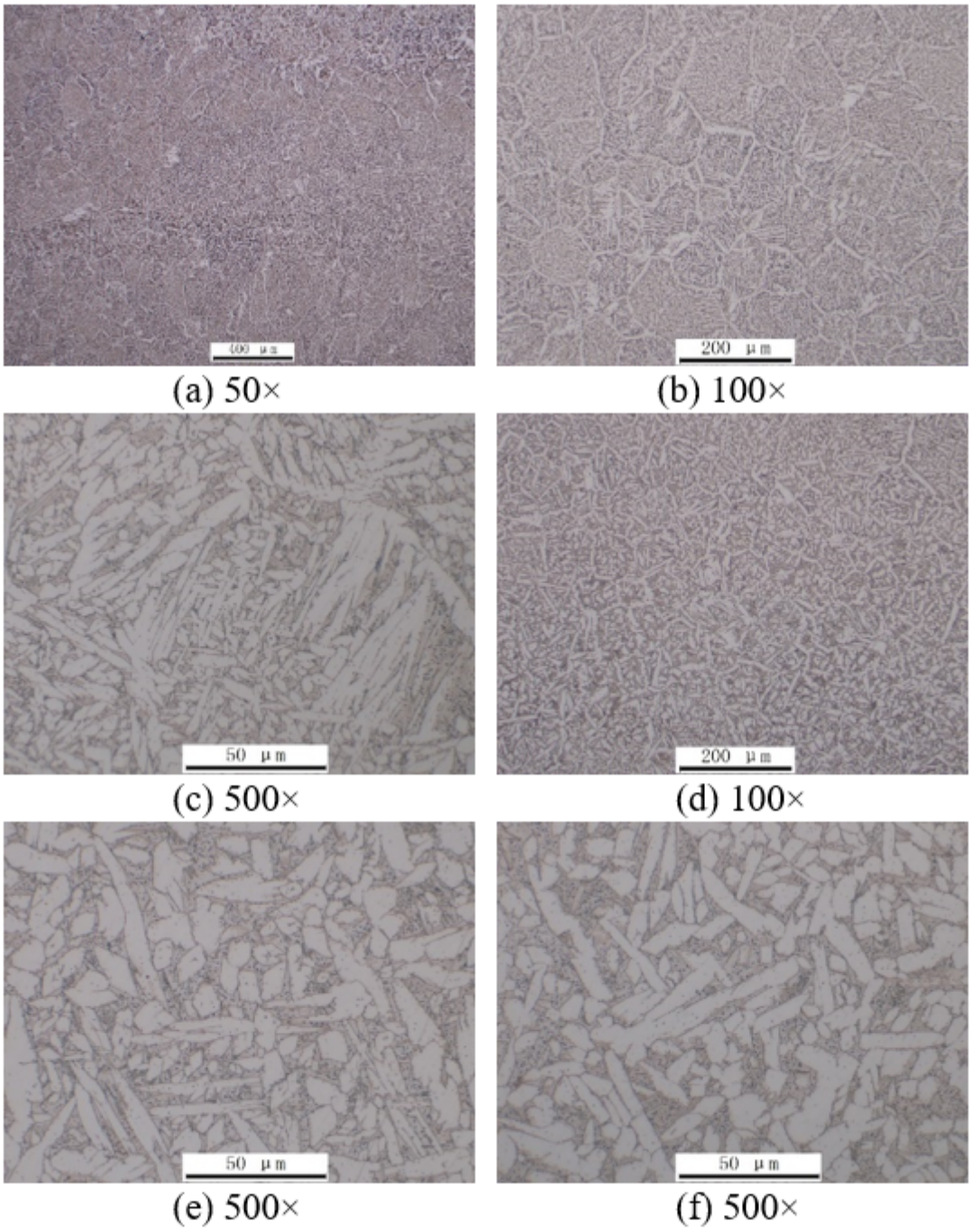


Figure 4

Microstructures of the specimens: (a) 50×, (b) equiaxed grain zone 100×, (c) equiaxed grain zone 500×, (d) remelting zone 100×, (e) remelting zone 500×, and (f) heat-affected zone 500×

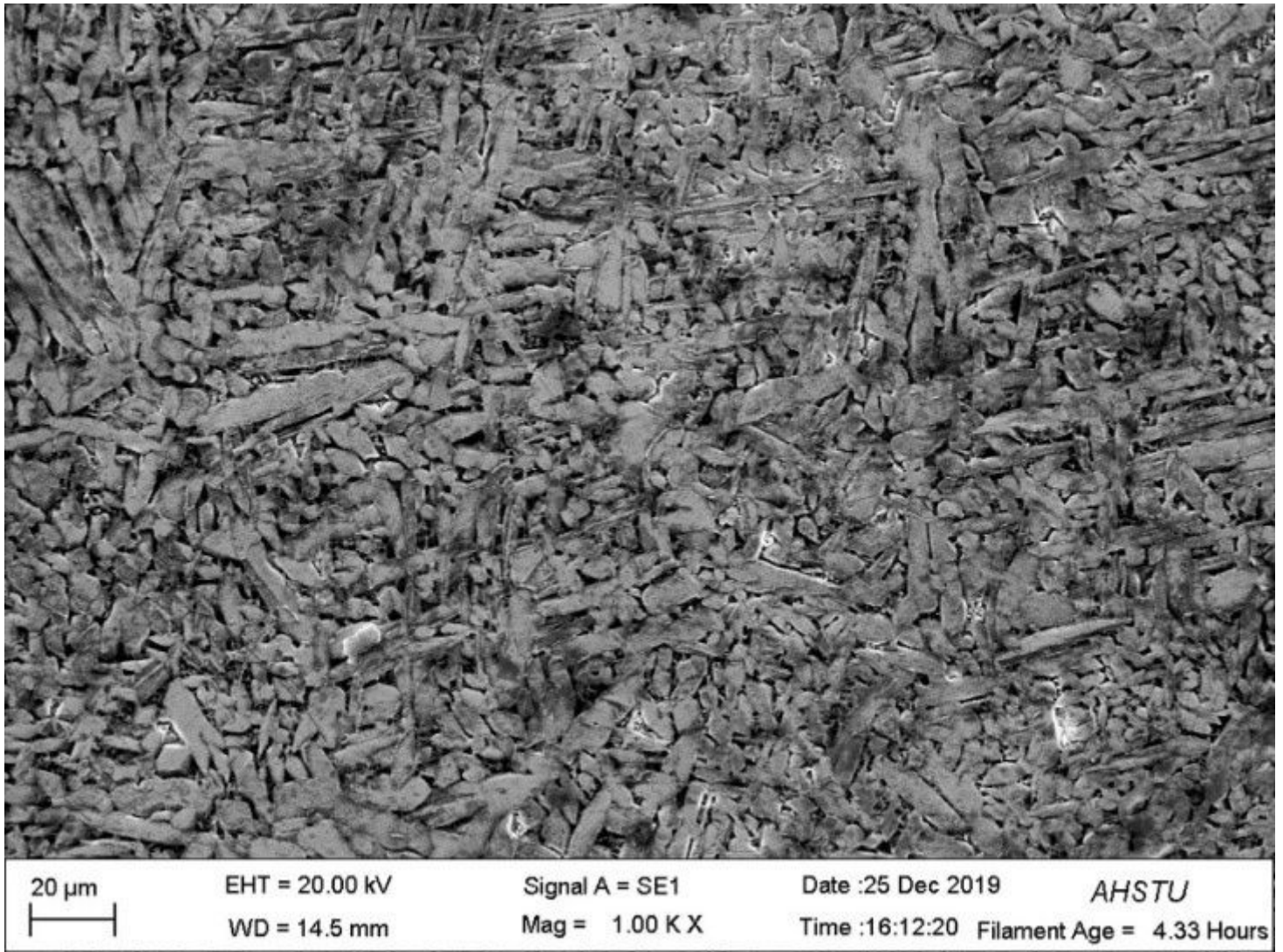
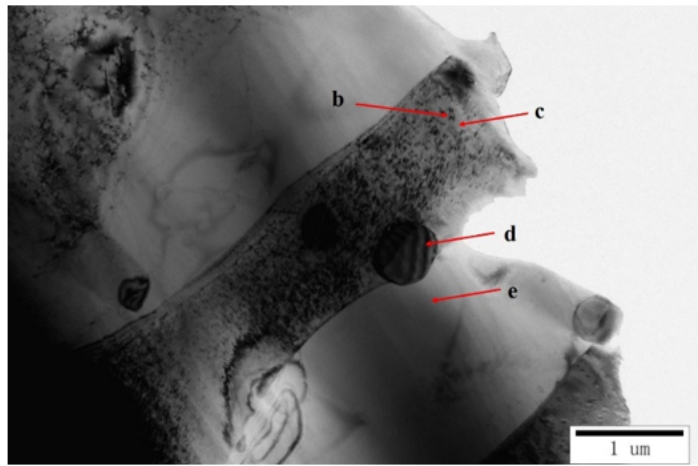
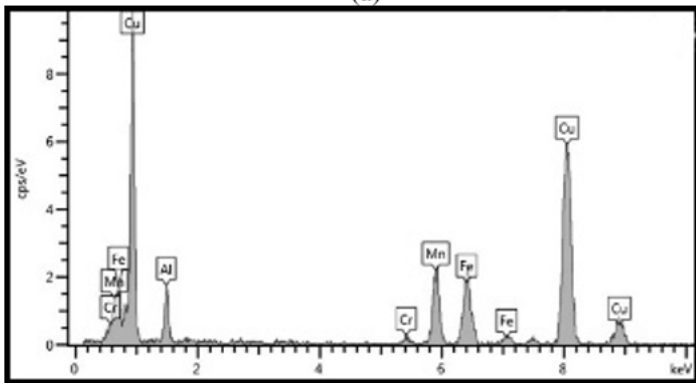


Figure 5

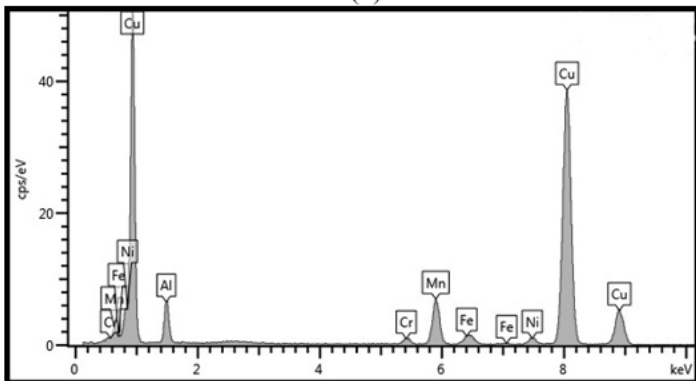
SEM image of the CuMn13Al7 sample formed by wire arc additive manufacturing



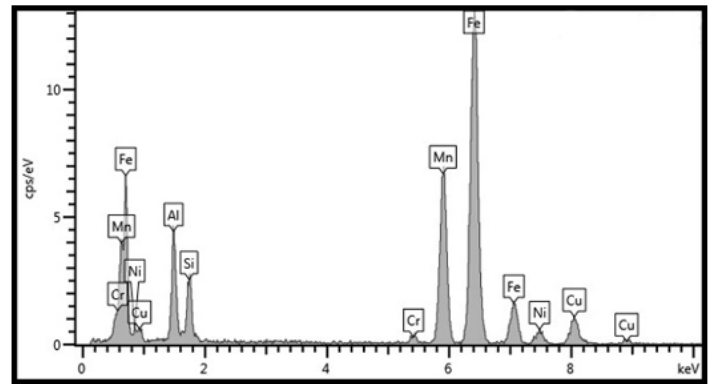
(a)



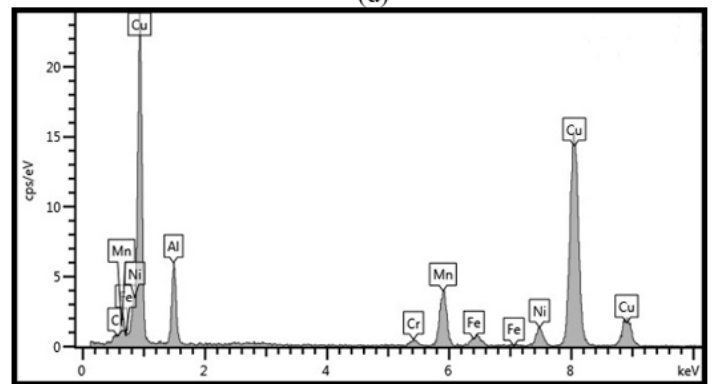
(b)



(c)



(d)



(e)

Figure 6

Microstructure data of the CuMn13Al7 sample formed by wire arc additive manufacturing: (a) overall morphology, (b) small particles and corresponding EDS, (c) dark matrix phase and corresponding EDS, (d) large particles and corresponding EDS, and (e) light matrix phase and corresponding EDS

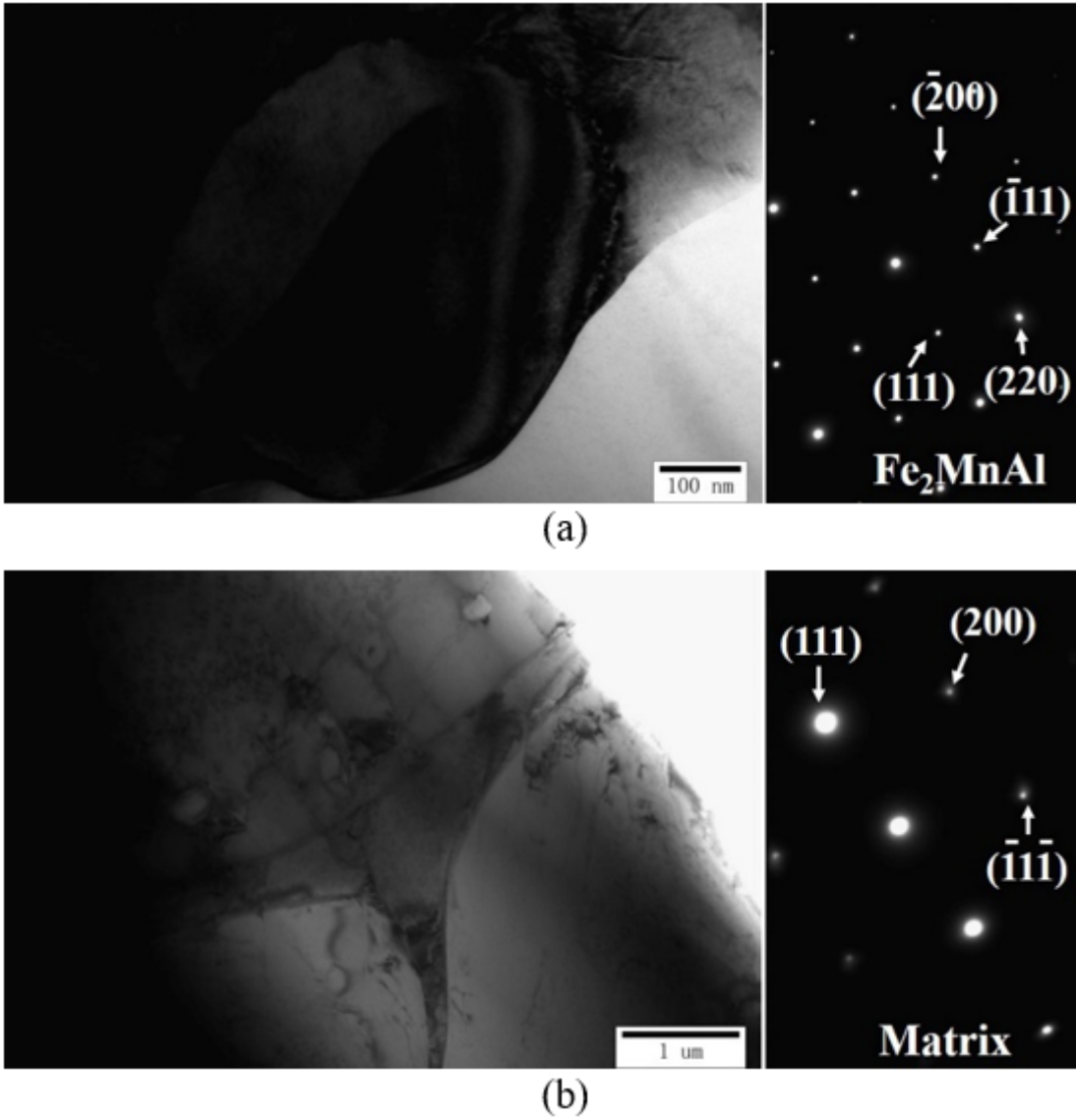


Figure 7

Microstructures of the CuMn13Al7 sample formed by wire arc additive manufacturing: (a) matrix and corresponding SAED; (b) matrix phase and corresponding SAED

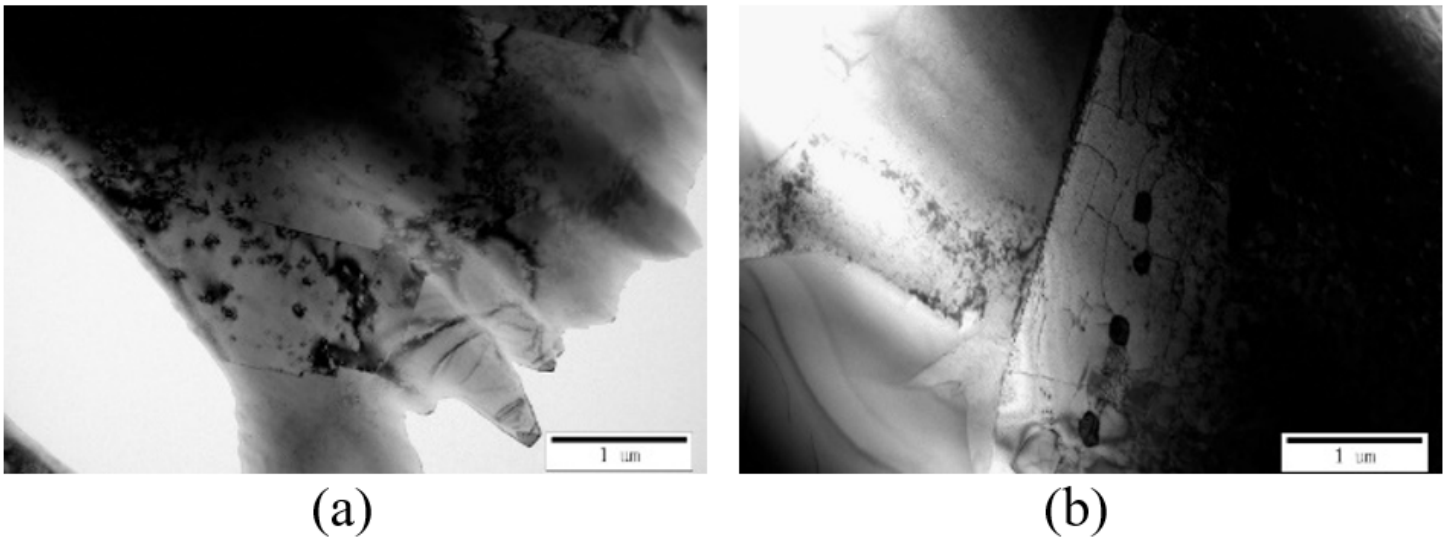


Figure 8

TEM image of the CuMn13Al7 sample formed by wire arc additive manufacturing: (a) particles + twin, (b) particles + dislocation

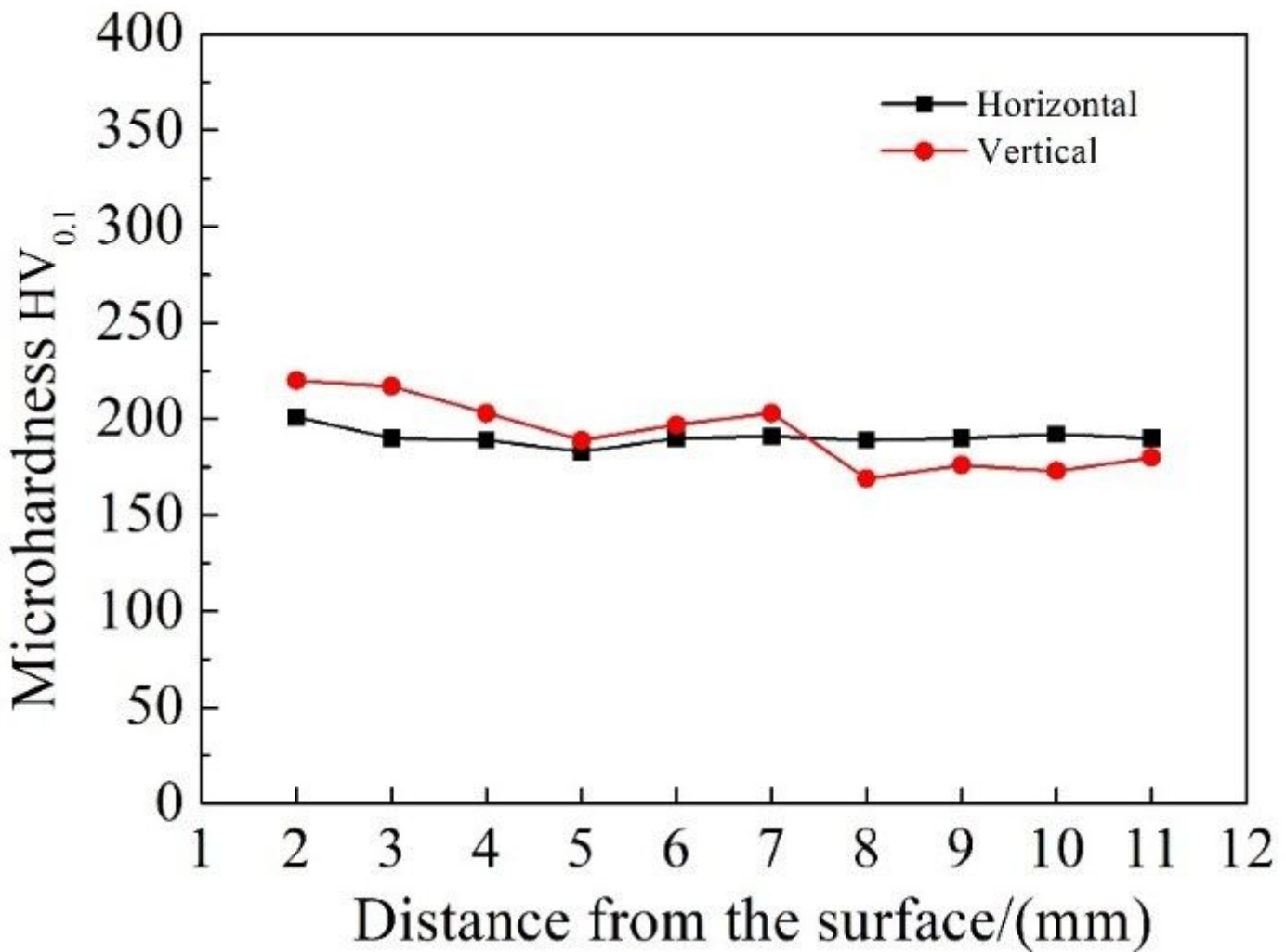


Figure 9



Figure 10

Tensile fracture morphology of the CuMn13Al7 sample made by wire arc additive manufacturing: (a) fracture appearance, (b) fibrous zone, (c) radical zone, (d) shear lip zone

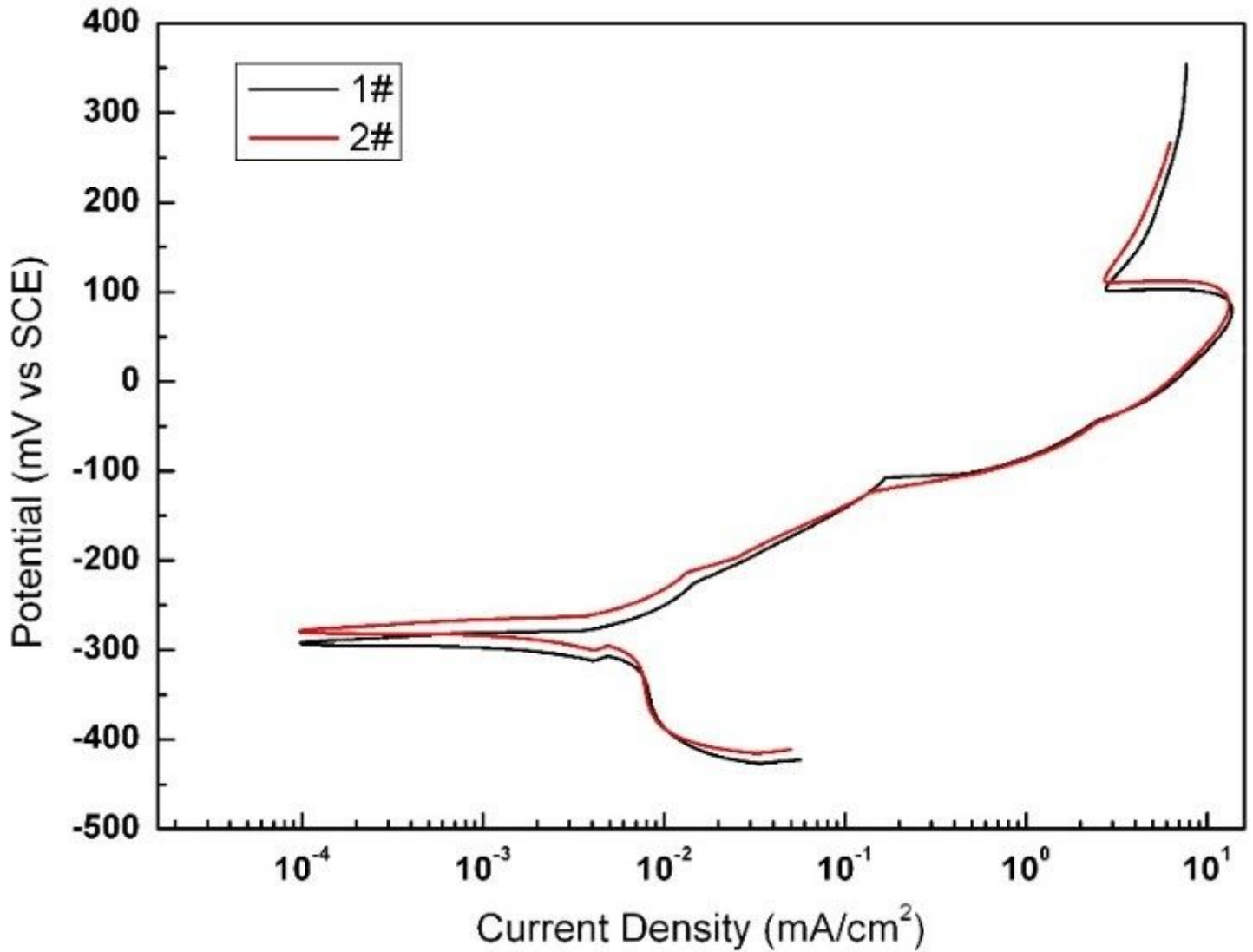
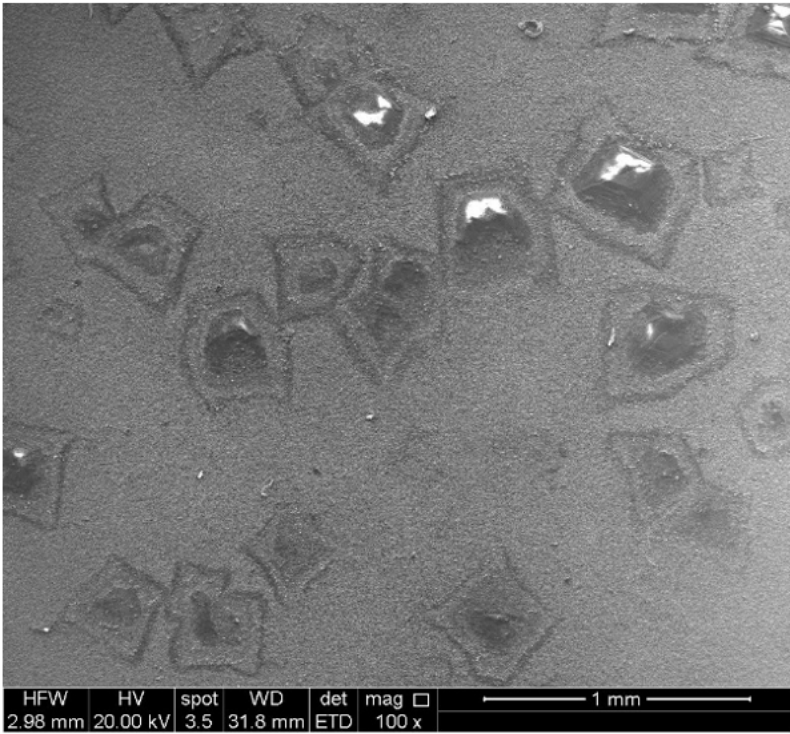
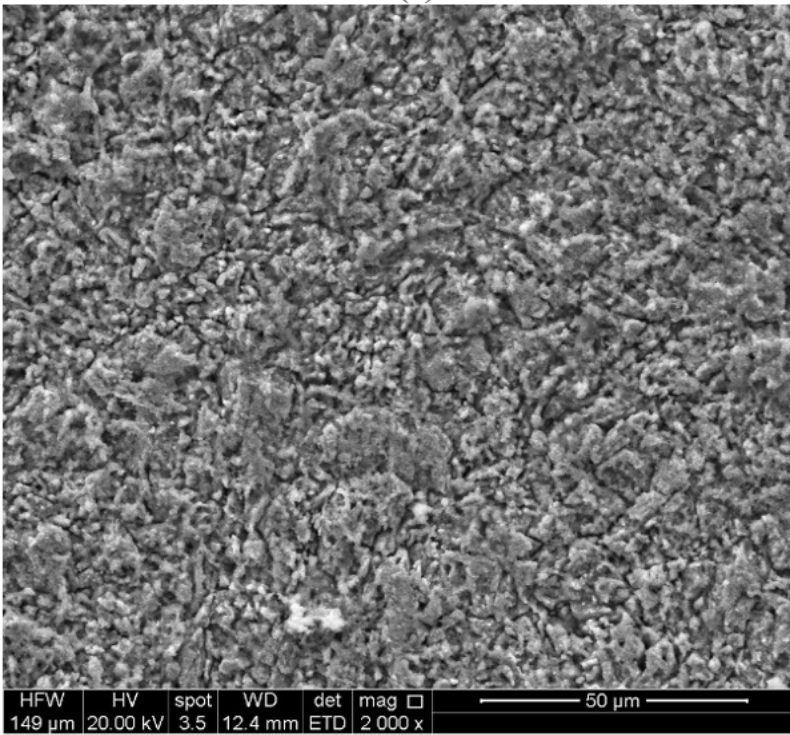


Figure 11

Potentiodynamic polarisation curves of the CuMn13Al7 sample formed by wire arc additive manufacturing in 3.5 wt% NaCl solution



(a)



(b)

Figure 12

Corroded morphologies of the CuMn13Al7 sample formed by wire arc additive manufacturing in 3.5 wt% NaCl solution